



Title	Effect of nonstoichiometry on the half-metallic character of Co ₂ MnSi investigated through saturation magnetization and tunneling magnetoresistance ratio
Author(s)	Li, Gui-fang; Honda, Yusuke; Liu, Hong-xi; Matsuda, Ken-ichi; Arita, Masashi; Uemura, Tetsuya; Yamamoto, Masafumi; Miura, Yoshio; Shirai, Masafumi; Saito, Toshiaki; Shi, Fengyuan; Voyles, Paul M.
Citation	Physical Review B, 89(1), 014428 https://doi.org/10.1103/PhysRevB.89.014428
Issue Date	2014-01-30
Doc URL	http://hdl.handle.net/2115/56328
Rights	© 2014 American Physical Society
Type	article
File Information	PhysRevB.89.014428.pdf



[Instructions for use](#)

Effect of nonstoichiometry on the half-metallic character of Co_2MnSi investigated through saturation magnetization and tunneling magnetoresistance ratio

Gui-fang Li, Yusuke Honda, Hong-xi Liu, Ken-ichi Matsuda, Masashi Arita, Tetsuya Uemura, and Masafumi Yamamoto*
*Division of Electronics for Informatics, Graduate School of Information Science and Technology, Hokkaido University,
 Sapporo 060-0814, Japan*

Yoshio Miura and Masafumi Shirai
Research Institute of Electrical Communication, Tohoku University, Sendai 980-8577, Japan

Toshiaki Saito
Department of Physics, Faculty of Science, Toho University, Funabashi 274-8510, Japan

Fengyuan Shi and Paul M. Voyles
Department of Materials Science and Engineering, University of Wisconsin-Madison, Madison, Wisconsin 53706-1595, USA
 (Received 9 July 2013; revised manuscript received 29 December 2013; published 30 January 2014)

We investigated the effect of nonstoichiometry on the half-metallic character of the Heusler alloy Co_2MnSi (CMS) through the Mn composition (α) dependence of the saturation magnetization per formula unit (μ_s) of $\text{Co}_2\text{Mn}_\alpha\text{Si}_\beta$ thin films and the tunneling magnetoresistance (TMR) ratio of CMS/MgO/CMS magnetic tunnel junctions (CMS MTJs) having $\text{Co}_2\text{Mn}_\alpha\text{Si}_\beta$ electrodes. As a basis for understanding the effect of nonstoichiometry in CMS, we developed a generalized form of the site-specific formula unit (SSFU) composition model, which assumes the formation of only antisite defects, not vacancies, to accommodate nonstoichiometry. The α dependence of μ_s was well explained by density functional calculations with the coherent potential approximation based on the SSFU composition model for α up to a certain critical value (α_c) > 1.0. The μ_s data for Mn-deficient films deviated from the Slater-Pauling predicted data for half-metals due to Co atoms at the nominal Mn sites (Co_{Mn}). The theoretical spin polarizations, obtained from only the s - and p -orbital components, $P_{\text{th}}(sp)$, were found to qualitatively explain the α dependence of the TMR ratio except for $\alpha > \alpha_c$. This is in contrast to the theoretical spin polarizations obtained from the s -, p -, and d -orbital components, $P_{\text{th}}(spd)$. A decrease in the TMR ratio observed for CMS MTJs having Mn-deficient electrodes was ascribed to small s - and p -orbital components of the local density of minority-spin in-gap states at the Fermi level that appeared for both antisite Co_{Mn} atoms and Co atoms at the regular sites.

DOI: [10.1103/PhysRevB.89.014428](https://doi.org/10.1103/PhysRevB.89.014428)

PACS number(s): 72.25.-b, 75.70.-i, 85.75.-d, 75.50.Cc

I. INTRODUCTION

Spintronic devices, which are based on the manipulation of the spin degree of freedom of the electron, have attracted much interest as future-generation electron devices [1] because of their potential advantages of nonvolatility, decreased power consumption, and reconfigurable logic function capabilities. A highly efficient spin source is essential for spintronic devices. Half-metallic ferromagnets (HMFs) are characterized by an energy gap for one spin direction, providing complete spin polarization at the Fermi level (E_F) [2]. Because of this characteristic, HMFs are one of the most suitable spin source materials for spintronic devices. Co-based Heusler alloys (Co_2YZ , where Y is usually a transition metal and Z is a main group element) [3] are among the most extensively applied to spintronic devices, including magnetic tunnel junctions (MTJs) [4–12] and giant magnetoresistance (GMR) devices [13–17] and for spin injection into semiconductors [18–20]. This is because of the theoretically predicted half-metallicity for many of them [21–23] and their high Curie temperatures, which are well above room temperature (RT) [24]. High-quality epitaxial heterostructures consisting of

a Co_2YZ thin film and a MgO tunnel barrier [7–11,25–30] or consisting of a Co_2YZ thin film and a thin nonmagnetic metal layer such as Ag have been prepared [13–16]. Furthermore, in epitaxial Co_2YZ/MgO heterostructures having a Co_2YZ electrode such as Co_2MnSi (CMS) and Co_2MnGe that have Δ_1 states in the majority spin band at E_F , coherent tunneling is dominant [31,32], leading to an enhancement of the tunneling spin polarization.

Among the Co_2YZ family, CMS has been one of the materials most extensively applied to MTJs [5–11,26–28] and GMR devices [13,15,16]. This is because of (1) its theoretically predicted half-metallic nature, with a large energy gap of 0.81 eV [22] for its minority-spin band; (2) its high Curie temperature of 985 K [24]; and (3) the existence of coherent tunneling in epitaxial CMS/MgO heterostructures [31,32]. On the other hand, nonstoichiometry is inevitable, to various degrees, in Co_2YZ thin films prepared by magnetron sputtering or molecular beam epitaxy, leading to structural defects. Thus, the clarification of the influence of structural defects on the half-metallicity of Co_2YZ is critical for spintronic device applications [33–36]. Picozzi *et al.* [33] theoretically predicted that Co_{Mn} antisites in CMS and Co_2MnGe , where a Mn site is replaced by a Co atom, cause minority-spin in-gap states at E_F and thus are detrimental to the half-metallicity of CMS and Co_2MnGe . Similarly, Miura *et al.* [34] theoretically predicted

*Corresponding author: yamamoto@nano.ist.hokudai.ac.jp

that disorder between Co sites and Cr sites in Co_2CrAl leads to a significant reduction in the spin polarization at E_F , while the disorder between Cr sites and Al sites does not significantly decrease the spin polarization. Some of us recently showed that the tunneling magnetoresistance (TMR) ratios at 4.2 K and at RT for epitaxial CMS/MgO/CMS MTJs (CMS MTJs) [8–10] and (from the bottom) $\text{Co}_{50}\text{Fe}_{50}/\text{MgO}/\text{CMS}$ MTJs [11] increased as the Mn composition in CMS was increased from Mn-deficient to Mn-rich. We demonstrated markedly high TMR ratios of 1995% at 4.2 K and 354% at RT for CMS MTJs with Mn-rich CMS electrodes [10]. The higher TMR ratios for MTJs with Mn-rich CMS electrodes were qualitatively explained by the suppression of the theoretically predicted Co_{Mn} antisites [8,9]. These results also demonstrated that a wide range of Mn-rich CMS films retain half-metallicity in terms of their Mn composition, which is also favorable for applying Co_2YZ thin films to spintronic devices. In this context, further understanding of the effect of nonstoichiometry on the electronic properties of CMS is important for extending the application of Heusler alloy films to spintronic devices.

The purpose of the present study was to elucidate the effect of nonstoichiometry on the half-metallic character of CMS. To do this, we investigated how the structural properties, the saturation magnetization per formula unit (μ_s), and the TMR ratio of CMS MTJs depend on the Mn composition in nonstoichiometric CMS thin films. Expressed as $\text{Co}_2\text{Mn}_\alpha\text{Si}_\beta$, the films had compositions with various Mn compositions α and a constant β for each film series. The structural properties of the films were experimentally investigated using the x-ray diffraction (XRD) intensity ratios of $I(002)/I(004)$ and $I(111)/I(022)$. As a basis for theoretically analyzing these experimental results, we developed a generalized form of the site-specific formula unit (SSFU) composition model [9], which assumes the formation of only antisite defects, not vacancies, to accommodate nonstoichiometry, resulting in the preservation of a 2:1:1 stoichiometry in terms of the $L2_1$ site occupation regardless of film nonstoichiometry in terms of the Co:Mn:Si atomic ratio.

The XRD intensity ratios of $I(002)/I(004)$ and $I(111)/I(022)$ provide insight into the site occupancy through a comparison with kinematical XRD theory calculations based on the SSFU compositions. The theoretical total spin magnetic moment per formula unit and the tunneling spin polarization at E_F for nonstoichiometric and stoichiometric $\text{Co}_2\text{Mn}_\alpha\text{Si}_\beta$ were calculated by first-principles calculations based on the SSFU composition. The experimental dependence of the XRD intensity ratios, μ_s , and the TMR ratio on α were consistently explained by the theoretical calculations for α ranging from that for a Mn-deficient composition to that for a certain Mn-rich composition, indicating the validity of the SSFU model based on the antisite formation for understanding the effect of nonstoichiometry in CMS.

This paper is organized as follows. Section II presents our experimental and computational methods, including the SSFU composition model. Section III presents the results and discussion. Section III A describes the structural properties of nonstoichiometric $\text{Co}_2\text{Mn}_\alpha\text{Si}_\beta$ films investigated through XRD and high-resolution atomic number (Z)-contrast scanning transmission electron microscopy (STEM). Section III B

describes the α dependence of μ_s of $\text{Co}_2\text{Mn}_\alpha\text{Si}_\beta$ thin films. Section III C describes the α dependence of the TMR ratios of CMS MTJs. In combination with the results of density functional theory calculations with coherent potential approximation (CPA), the experimental dependence of μ_s and the TMR ratio on α is discussed in terms of the effect of defects associated with nonstoichiometry on the half-metallic character of CMS. Section III C also describes the experimental dependence on α of the degree of temperature dependence of the TMR ratio of CMS MTJs and its origin. Section IV summarizes our results and concludes the paper.

II. EXPERIMENTAL AND COMPUTATIONAL METHODS

A. Experimental method

In order to investigate the effect of nonstoichiometry on the structural and magnetic properties of CMS thin films, we prepared $\text{Co}_2\text{Mn}_\alpha\text{Si}_\beta$ films having various values of α and a constant value of β for each film series. The sample layer structure we prepared for the magnetization measurements and structural characterization by XRD and STEM was as follows: (from the substrate side) MgO buffer (10 nm)/CMS (~30 nm)/MgO barrier (2 nm)/ AlO_x cap layer (1 nm), grown on a MgO(001) substrate, as shown in Fig. 1. This layer structure corresponds to half of an MTJ. We used a MgO barrier to protect the CMS surface because we had previously confirmed that the CMS layer is not oxidized by MgO deposition by means of x-ray absorption spectroscopy and x-ray magnetic circular dichroism [37] and because of the demonstrated high quality of the CMS/MgO interface [10,11].

The CMS thin film was deposited at RT using radio-frequency magnetron cosputtering from a nearly

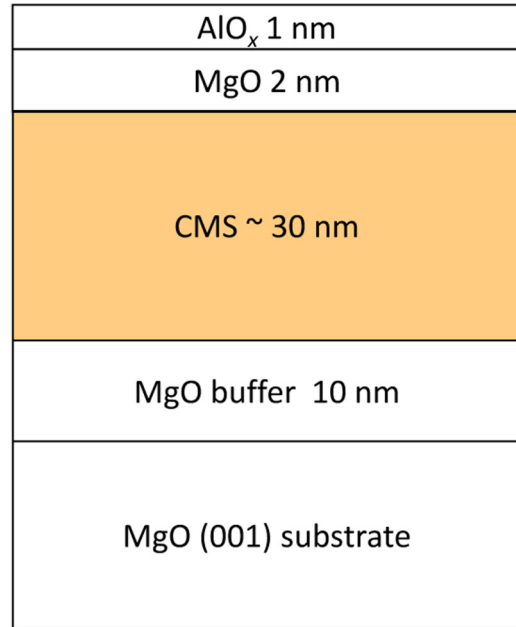


FIG. 1. (Color online) Schematic of the layer structure consisting of (from the substrate side) MgO buffer (10 nm)/ $\text{Co}_2\text{Mn}_\alpha\text{Si}_\beta$ /MgO barrier (2 nm)/ AlO_x cap layer (1 nm) grown on a MgO(001) substrate. The layer structure corresponds to half of an MTJ. The thicknesses of $\text{Co}_2\text{Mn}_\alpha\text{Si}_\beta$ layers are about 30 nm.

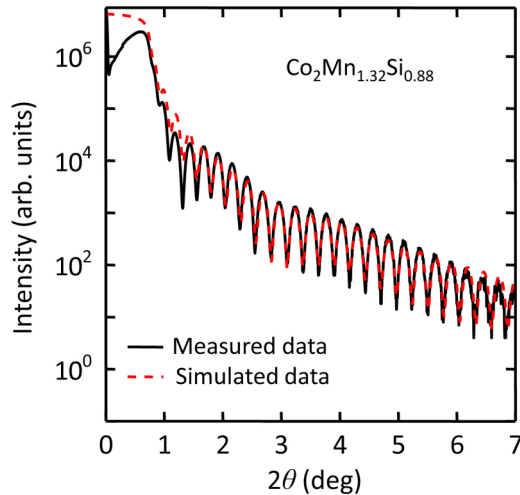


FIG. 2. (Color online) A typical low-angle x-ray reflectivity scan for a layer structure consisting of MgO(001) substrate/MgO buffer (10 nm)/Co₂Mn_{1.32}Si_{0.88} thin layer/MgO barrier (2 nm)/AlO_x cap layer (1 nm). The solid and dotted lines represent the experimental and fitted curves as a function of angle 2θ . A fit of the oscillatory x-ray reflectivity intensity was done for a 2θ range from 1.4 to 5.6°. Through fitting, the Co₂Mn_{1.32}Si_{0.88} layer thickness was determined to be 32.34 nm.

stoichiometric CMS target and Mn target and was subsequently annealed *in situ* at 600 °C for 15 min. The Mn composition α in the Co₂Mn _{α} Si _{β} was systematically varied by adjusting the relative amount of Mn sputtered from a Mn target by cosputtering.

We determined the film composition of the prepared CMS films by inductively coupled plasma analysis with an accuracy of 2–3% for each element except Si, for which the accuracy was 5%.

The saturation magnetization per formula unit, μ_s , was measured at 10 K for two series of Co₂Mn _{α} Si _{β} films with a variable α and a fixed β of 0.88 or 1.0. The saturation magnetization, M_s , of each film at 10 K was estimated by an extrapolation of the M - H curve measured using a superconducting quantum interference device magnetometer to $H = 0$ to subtract the contribution from the MgO substrate. Determining μ_s from the M_s value for comparison with theoretical calculations requires precise determination of the film thicknesses, which we measured using low-angle x-ray reflectivity. A typical low-angle x-ray reflectivity scan for a layer structure consisting of MgO(001) substrate/MgO buffer (10 nm)/Co₂Mn_{1.32}Si_{0.88} (~30 nm)/MgO barrier

(2 nm)/AlO_x cap layer (1 nm) is shown in Fig. 2. The solid and dotted lines are the experimental and fitted curves plotted as a function of angle 2θ . Clear oscillations in the experimental reflectivity scan observed up to $2\theta \sim 7^\circ$ revealed smooth interfaces and surface. A fit of the oscillatory x-ray reflectivity intensity for a 2θ range from 1.4 to 5.6° (dotted line) using the Parratt formalism [38] yielded a Co₂Mn_{1.32}Si_{0.88} layer thickness of 32.34 nm for this film. This method was used to determine the thickness of each Co₂Mn _{α} Si _{β} layer.

The lattice constants in the plane, a , and perpendicular to the plane, c , also had to be determined for the films in order to obtain μ_s . a and c were measured by making x-ray θ - 2θ Bragg scans with a four-axis x-ray diffractometer (Bruker AXS D8 Discover Hybrid) with a scintillation counter. Tables I and II show the measured values of a and c for Co₂Mn _{α} Si_{1.0} films and Co₂Mn _{α} Si_{0.88} films, respectively. For the Co₂Mn _{α} Si_{1.0} films, a increased from $a = 0.564$ nm for $\alpha = 0.69$ to $a = 0.567$ nm for $\alpha = 1.44$ (0.5% increase in a), while c was almost constant and showed only an increase within 0.1% for a range of α from 0.69 to 1.44 (Table I). The measured a (=0.5664 nm) and c (=0.5649 nm) for a stoichiometric Co₂Mn_{1.0}Si_{1.0} film (Table I) are in good agreement with the a (=0.5654 nm) reported for a polycrystalline CMS bulk sample [24]. The measured a and c for the Co₂Mn _{α} Si_{0.88} films showed a similar dependence on α (Table II).

To investigate the site occupancies of the nonstoichiometric Co₂Mn _{α} Si _{β} films, we measured the ratio of the 002 peak intensity with respect to the 004 peak intensity, $I(002)/I(004)$, and the ratio of the 111 peak intensity to the 022 peak intensity, $I(111)/I(022)$, in XRD. The 002 peak is characteristic of the $B2$ and $L2_1$ structures, the 111 peak is characteristic of the $L2_1$ structure, and the 004 and 022 peaks are characteristic to the fundamental $A2$ structure. For these measurements, we used a two-dimensional position-sensitive proportional counter (two-dimensional detector) in the four-axis x-ray diffractometer. The sample rotation angle (φ), tilt angle (χ), incident angle (ω), and detection angle (or diffraction angle) (2θ) were fixed in the diffraction intensity measurement using the two-dimensional detector. However, the intensity profiles along χ and 2θ were included in the measured intensities due to the use of the two-dimensional detector. In XRD intensity ratio measurements, the x-ray irradiation area, which depends on the incident angle of the x rays, must be smaller than the sample size for any diffraction angles to be investigated. An x-ray collimator having a beam diameter of 0.5 mm was used for the measurements using the two-dimensional detector, thereby ensuring this condition was met for all 002, 004, 111, and 022 reflections.

TABLE I. SSFU compositions, formula unit type, and measured lattice parameters a and c for ~30-nm-thick epitaxial Co₂Mn _{α} Si_{1.0} films with various Mn compositions α grown on MgO(001) substrates.

α in Co ₂ Mn _{α} Si _{1.0}	SSFU composition	Type no.	a (nm)	c (nm)
0.69	Co ₂ [Mn _{0.75} Co _{0.17} Si _{0.08}]Si	I	0.5643	0.5648
0.85	Co ₂ [Mn _{0.88} Co _{0.08} Si _{0.04}]Si	I	0.5658	0.5647
1.00	Co ₂ MnSi	–	0.5664	0.5649
1.15	[Co _{1.93} Mn _{0.07}]Mn[Si _{0.96} Mn _{0.04}]	III	0.5670	0.5647
1.29	[Co _{1.86} Mn _{0.14}]Mn[Si _{0.93} Mn _{0.07}]	III	0.5672	0.5653
1.44	[Co _{1.80} Mn _{0.20}]Mn[Si _{0.90} Mn _{0.10}]	III	0.5674	0.5654

TABLE II. SSFU compositions, formula unit type, and measured lattice parameters a and c for ~ 30 -nm-thick epitaxial $\text{Co}_2\text{Mn}_\alpha\text{Si}_{0.88}$ films with various Mn compositions α grown on MgO(001) substrates.

α in $\text{Co}_2\text{Mn}_\alpha\text{Si}_{0.88}$	SSFU composition	Type no.	a (nm)	c (nm)
0.72	$\text{Co}_2[\text{Mn}_{0.78}\text{Co}_{0.22}][\text{Si}_{0.98}\text{Mn}_{0.02}]$	II	0.5642	0.5652
1.00	$\text{Co}_2[\text{Mn}_{0.94}\text{Co}_{0.06}][\text{Si}_{0.91}\text{Mn}_{0.09}]$	II	0.5657	0.5655
1.15	$[\text{Co}_{1.99}\text{Mn}_{0.01}]\text{Mn}[\text{Si}_{0.88}\text{Mn}_{0.12}]$	III	0.5667	0.5655
1.32	$[\text{Co}_{1.90}\text{Mn}_{0.10}]\text{Mn}[\text{Si}_{0.84}\text{Mn}_{0.16}]$	III	0.5666	0.5651
1.37	$[\text{Co}_{1.88}\text{Mn}_{0.12}]\text{Mn}[\text{Si}_{0.83}\text{Mn}_{0.17}]$	III	0.5672	0.5654
1.53	$[\text{Co}_{1.81}\text{Mn}_{0.19}]\text{Mn}[\text{Si}_{0.80}\text{Mn}_{0.20}]$	III	0.5680	0.5660
1.68	$[\text{Co}_{1.75}\text{Mn}_{0.25}]\text{Mn}[\text{Si}_{0.77}\text{Mn}_{0.23}]$	III	0.5673	0.5659
1.84	$[\text{Co}_{1.69}\text{Mn}_{0.31}]\text{Mn}[\text{Si}_{0.75}\text{Mn}_{0.25}]$	III	0.5672	0.5657

The lower and upper CMS electrodes in the MTJ layer structures were also characterized by (1) reflection high-energy electron diffraction (RHEED) observations during growth, (2) cross-sectional high-resolution transmission electron microscope lattice image observations, (3) electron diffraction observations, and (4) aberration-corrected Z-contrast STEM. High-resolution STEM (HRSTEM) was performed on an FEI Titan STEM with a CEOS probe aberration corrector operated at 200 kV with ~ 0.1 -nm spatial resolution, 24.5-mrad convergence angle, and 25-pA probe current. The high-angle annular dark-field detector subtended 54 to 270 mrad. All the HRSTEM images were smoothed with a Gaussian filter smaller than the 0.1-nm instrumental resolution to reduce shot noise. The STEM samples were prepared by the tripod polishing [39], then finished by ion milling.

We defined the TMR ratio as $(R_{\text{AP}} - R_{\text{P}})/R_{\text{P}}$, where R_{AP} and R_{P} are the tunneling resistances at a small dc voltage for the antiparallel and parallel magnetization configurations between the upper and lower electrodes.

B. Computational method

To investigate the effect of α on the electronic properties, we performed density functional calculations on the basis of the Korringa-Kohn-Rostoker (KKR) method [40,41] with the CPA to determine the total magnetic moments per formula unit, m_{spin} , and the spin-resolved, local density of states (LDOS). In this method, the space is divided into nonoverlapping muffin-tin spheres. We used a scalar relativistic calculation, in which the spin-orbit interaction was neglected. For the Brillouin zone (BZ) integration, we included 8000 points in the full BZ. The unit cell of the full-Heusler alloy X_2YZ with the L_{21} structure consists of four different fcc sublattices. Each has an atom basis as follows: X element at $(1/4, 1/4, 1/4)$ and $(3/4, 3/4, 3/4)$, Y at $(0,0,0)$, and Z at $(1/2, 1/2, 1/2)$. We used the generalized gradient approximation for the exchange and correlation term [42]. We used the experimental lattice constants a described above for both $\text{Co}_2\text{Mn}_\alpha\text{Si}_{1.0}$ films (Table I) and $\text{Co}_2\text{Mn}_\alpha\text{Si}_{0.88}$ films (Table II), but we ignored the small difference between a and c and assumed a cubic CMS lattice with the experimental a value for each film. The KKR-CPA calculations were based on the SSFU composition model assuming antisite formation rather than vacancy formation to accommodate nonstoichiometry, as described in Sec. II C.

C. Formula unit composition model

In our previous paper [9], we proposed a model of the SSFU composition for nonstoichiometric $\text{Co}_2\text{Mn}_\alpha\text{Si}_\beta$. In this section, we describe the model from a more generalized point of view. This model emphasizes the occupancy at each site in the L_{21} lattice, rather than simply describing the compositions of Co, Mn, and Si atoms included in the formula unit. Most importantly, we assumed the formation of antisite defects, not vacancies, to accommodate nonstoichiometry. This is because of the theoretically predicted higher formation energies of vacancies at the nominal Co, Mn, and Si sites compared with various kinds of antisites for CMS [33,36]. In this model, each site in the L_{21} structure is occupied, either by the nominal atom (Co, Mn, or Si) for that site or by an antisite defect atom, so the total number of atoms included in the formula unit, $N_{f.u.}$, is always four, even though the film is nonstoichiometric in terms of the Co:Mn:Si atomic ratio. Thus, this model preserves a generalized 2:1:1 stoichiometry in terms of the site occupancy. We call this SSFU composition model the antisite-based SSFU composition model.

Given this model, we showed three types of SSFU compositions, summarized in Table III, which cover all the formula unit compositions of the films that we investigated in this paper. These films include $\text{Co}_2\text{Mn}_\alpha\text{Si}_{1.0}$ with a Co:Si ratio of 2:1 and Si-deficient $\text{Co}_2\text{Mn}_\alpha\text{Si}_\beta$ with $\beta < 1.0$, both over a range of α from a Mn-deficient composition ($\alpha < 2 - \beta$) to a Mn-rich one ($\alpha > 2 - \beta$).

Let us first consider $\text{Co}_2\text{Mn}_\alpha\text{Si}_{1.0}$ ($\beta = 1.0$). For $\alpha < 1$ (Mn deficient), some of the Mn sites are filled by surplus Co and Si atoms, creating Co_{Mn} and Si_{Mn} antisites, both of which have lower calculated formation energy than Mn vacancies [33,36]. The resulting SSFU composition is $\text{Co}_2[\text{Mn}_{1-x-y}\text{Co}_x\text{Si}_y]\text{Si}$, which we call a type I SSFU composition. $[\text{Mn}_{1-x-y}\text{Co}_x\text{Si}_y]$

TABLE III. General expressions for the SSFU compositions of type I to type III for $\text{Co}_2\text{Mn}_\alpha\text{Si}_\beta$ with the restrictions $0 < \alpha < 2$ and $0 < \beta < 2$.

Type no.	General expression for SSFU composition	x	y
I	$\text{Co}_2[\text{Mn}_{1-x-y}\text{Co}_x\text{Z}_y]\text{Z}$	$\frac{2(2-(\alpha+\beta))}{2+\alpha+\beta}$	$\frac{3\beta-(2+\alpha)}{2+\alpha+\beta}$
II	$\text{Co}_2[\text{Mn}_{1-x}\text{Co}_x][\text{Z}_{1-y}\text{Mn}_y]$	$\frac{2(2-(\alpha+\beta))}{2+\alpha+\beta}$	$\frac{2+\alpha-3\beta}{2+\alpha+\beta}$
III	$[\text{Co}_{2-x}\text{Mn}_x]\text{Mn}[\text{Z}_{1-y}\text{Mn}_y]$	$\frac{2(\alpha+\beta-2)}{2+\alpha+\beta}$	$\frac{2+\alpha-3\beta}{2+\alpha+\beta}$

is the composition on the nominal Mn site. For $\alpha > 1$ (Mn-rich), the excess Mn atoms occupy nominal Co and Si sites, creating Mn_{Co} and Mn_{Si} antisites, both of which have lower calculated formation energy than either a Co or Si site vacancy [33,36]. The resulting SSFU composition is $[\text{Co}_{2-x}\text{Mn}_x]\text{Mn}[\text{Si}_{1-y}\text{Mn}_y]$, which we call type III. $[\text{Co}_{2-x}\text{Mn}_x]$ and $[\text{Si}_{1-y}\text{Mn}_y]$ are the compositions of the nominal Co and Si sites, respectively.

Next, let us consider Si-deficient $\text{Co}_2\text{Mn}_\alpha\text{Si}_\beta$ ($\beta < 1.0$). Again, there are two cases, determined by the Co atomic ratio in the formula unit, r_{Co} . The ratio r_{Co} is given by $2/N = 2/(2 + \alpha + \beta)$, where the number of Co atoms included in one unit of $\text{Co}_2\text{Mn}_\alpha\text{Si}_\beta$, 2, is divided by the total number of atoms included in one unit of $\text{Co}_2\text{Mn}_\alpha\text{Si}_\beta$, $N = 2 + \alpha + \beta$. ($N = N_{f.u.} = 4$ only for $\alpha + \beta = 2$.) If $r_{\text{Co}} > 1/2$ (i.e., $\alpha + \beta < 2$), some of the Si sites are filled by Mn atoms, creating Mn_{Si} antisites, which have lower predicted formation energy than Co_{Si} antisites [36], and some of the Mn sites are filled by Co atoms, creating Co_{Mn} antisites, which have lower formation energy than Mn vacancies [36]. This results in a type II SSFU composition of $\text{Co}_2[\text{Mn}_{1-x}\text{Co}_x][\text{Si}_{1-y}\text{Mn}_y]$. If $r_{\text{Co}} < 1/2$ (i.e., $\alpha + \beta > 2$), which is the case for Mn-rich $\text{Co}_2\text{Mn}_\alpha\text{Si}_\beta$ with $\alpha > 2 - \beta$ and $\beta < 1$, the SSFU composition is of type III.

The parameters x and y in the SSFU composition are determined as functions of α and β from the requirement that the Co:Mn:Si atomic ratio in the resulting formula unit composition must be equal to the film composition expressed as $\text{Co}_2\text{Mn}_\alpha\text{Si}_\beta$ with given α and β . Furthermore, the boundaries of the respective regions of the type I to type III SSFU compositions in the α - β plane are determined from the requirements that the parameters x and y should be in the range of $0 < x < 1$, and $0 < y < 1$ [Fig. 3]. The boundary given by $\alpha + \beta = 2$ corresponds to the SSFU composition, where r_{Co} is $1/2$. Similarly, the boundary given by $\beta = (2 + \alpha)/3$ corresponds to the SSFU composition, where the Si atomic ratio in the formula unit, r_{Si} , given by $r_{\text{Si}} = \beta/(2 + \alpha + \beta)$, is $1/4$. Thus, the Co atomic ratio in the formula unit for the type I and type II regions in the α - β plane is larger than $1/2$ and that for the type III region is smaller than $1/2$.

The calculated SSFU compositions of the samples are listed in Table I for $\beta = 1.0$ and in Table II for $\beta = 0.88$. We used these compositions to model various experiment results, including structural properties, μ_s , and TMR ratios, in order to test whether the underlying assumption of dominant antisite defects is true and to explore the effect of such antisite defects on the half-metallic character of $\text{Co}_2\text{Mn}_\alpha\text{Si}_\beta$.

III. RESULTS AND DISCUSSION

A. Structural properties

First, we describe the effects of nonstoichiometry on the structural properties of $\text{Co}_2\text{Mn}_\alpha\text{Si}_\beta$ films having various α values with a fixed β for each series. RHEED observations of these nonstoichiometric CMS films showed $1/2$ -order superlattice reflections (or 11^* streak lines) along the $[110]_{\text{CMS}}$ direction for both the Mn-deficient and Mn-rich compositions, as has been shown for a Mn-deficient $\text{Co}_2\text{Mn}_{0.91}\text{Si}_{0.93}$ film [26] and for a Mn-rich $\text{Co}_2\text{Mn}_{1.29}\text{Si}_{1.0}$ film [11], indicating $L2_1$

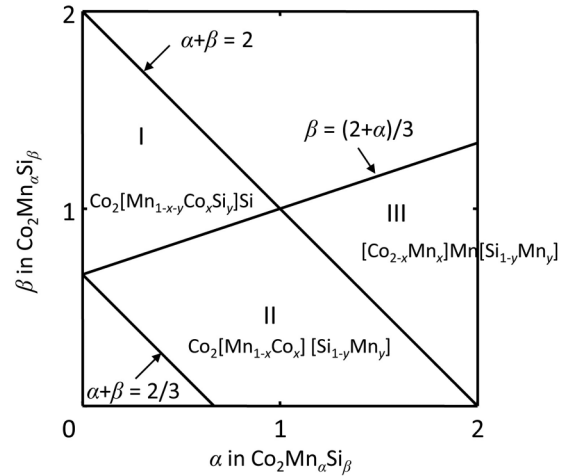


FIG. 3. Schematic diagram showing the regions of the SSFU composition types I to III in the α - β plane for $\text{Co}_2\text{Mn}_\alpha\text{Si}_\beta$ with the restrictions of $0 < \alpha < 2$ and $0 < \beta < 2$. The parameters x and y for each type are given as functions of α and β in Table III. The boundary given by $\alpha + \beta = 2$ corresponds to the formula unit composition where the Co atomic ratio in the formula unit is $1/2$. Similarly, the boundary given by $\beta = (2 + \alpha)/3$ corresponds to the formula unit composition, where the Si atomic ratio is $1/4$, and that given by $\alpha + \beta = 2/3$ corresponds to the formula unit composition, where the Co atomic ratio is $3/4$.

order at the surface of the prepared nonstoichiometric CMS films regardless of whether their composition was Mn-rich or Mn-deficient. The electron diffraction patterns for both a Mn-deficient CMS film having a film composition of $\text{Co}_2\text{Mn}_{0.91}\text{Si}_{0.93}$ [43] and a Mn-rich CMS film having that of $\text{Co}_2\text{Mn}_{1.29}\text{Si}_{1.0}$ [9] showed 111 spots, indicating the existence of the $L2_1$ structure in both the films.

Figures 4(a) and 4(b) show the measured intensity ratios $I(002)/I(004)$ and $I(111)/I(022)$ for four samples of $\text{Co}_2\text{Mn}_\alpha\text{Si}_{0.88}$ films with $\alpha = 0.72, 1.0, 1.37,$ and 1.84 . The respective SSFU compositions for these four samples are shown in Table II.

$I(002)/I(004)$ decreased monotonically with increasing α . Furthermore, $I(111)/I(022)$ for $\alpha = 1.0, 1.37,$ and 1.84 were clearly lower than that for $\alpha = 0.72$. The atomic scattering factors of the Mn atom (the atomic number 25) and Co atom (27) are close, but that of the Si atom (14) is about half that of Mn and Co, so the 002 peak intensity for CMS in the XRD mainly depends on the occupation ratio of Si in the MnSi plane (γ_1). According to the SSFU compositions for $\text{Co}_2\text{Mn}_\alpha\text{Si}_{0.88}$, γ_1 decreases with increasing α from $\gamma_1 = 0.98/2$ for $\alpha = 0.72$ to $\gamma_1 = 0.75/2$ for $\alpha = 1.84$. Thus, the observed decrease in $I(002)/I(004)$ can be ascribed to the decrease in the occupation of Si in the MnSi plane with increasing α , as shown by the SSFU compositions. Similarly, the 111 peak intensity for CMS mainly depends on the occupation of Si at the nominal Si site (γ_2), and the γ_2 values for $\alpha = 1.0, 1.37,$ and 1.84 ranging from $\gamma_2 = 0.91$ for $\alpha = 1.0$ to $\gamma_2 = 0.75$ for $\alpha = 1.84$ are definitely lower than the $\gamma_2 = 0.98$ for $\alpha = 0.72$. Thus, the observed $I(111)/I(022)$ being lower for $\alpha = 1.0, 1.37,$ and 1.84 than for $\alpha = 0.72$ can also be attributed to the lower occupation of Si

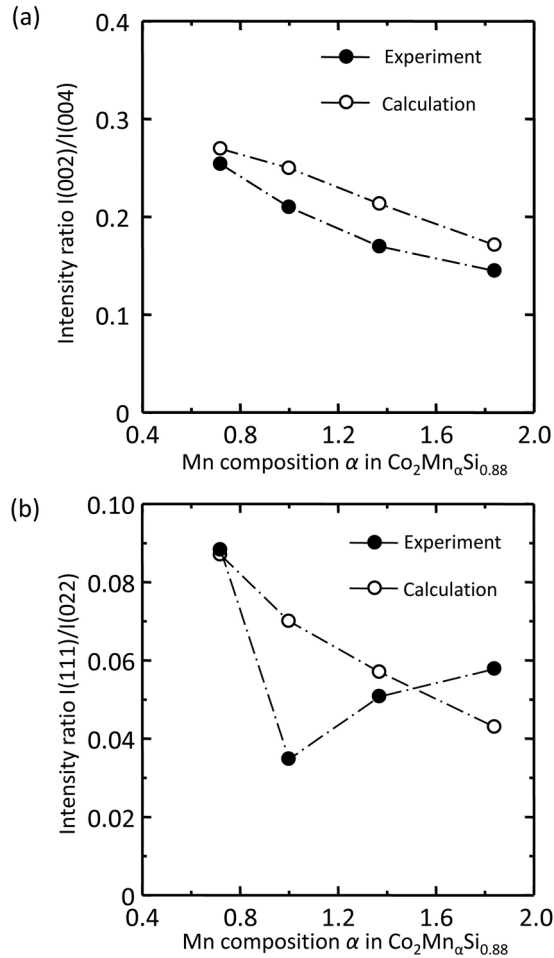


FIG. 4. Mn composition (α) dependence in $\text{Co}_2\text{Mn}_\alpha\text{Si}_{0.88}$ films of the experimental (solid circles) and calculated (open circles) ratios of XRD intensity of (a) 002 peak with respect to that of 004 peak, $I(002)/I(004)$ and (b) 111 peak with respect to that of 022 peak, $I(111)/I(022)$. The calculated ratios were obtained using the kinematical XRD theory and formula unit compositions given in Table II.

in the MnSi plane for $\alpha = 1.0, 1.37,$ and 1.84 , as shown by the SSFU compositions.

We also calculated $I(002)/I(004)$ and $I(111)/I(022)$ for $\text{Co}_2\text{Mn}_\alpha\text{Si}_{0.88}$ as a function of α using kinematical XRD theory and the SSFU compositions. Although the main factor in the calculation is the structure factor that depends on the site occupations, we also took into account (1) the Lorentz factor proportional to $1/\sin(2\theta)$ for a single-crystalline film, (2) the polarization factor proportional to $1+\cos^2 2\theta$, and (3) the absorption factor proportional to $(1-\exp(-2\mu t/\sin\theta))$, where t is a film thickness smaller than the effective x-ray penetration depth, and μ is the line absorption coefficient of the film. The calculated $I(002)/I(004)$ and $I(111)/I(022)$, shown in Figs. 4(a) and 4(b), decreased with increasing α . Thus, we found a fairly good agreement between the experimental and calculated dependences of $I(002)/I(004)$, indicating the validity of the proposed SSFU compositions, in particular, regarding the order between the nominal Co plane and the nominal MnSi plane.

For $I(111)/I(022)$, which is related to the order between the nominal Mn site and the nominal Si site in the MnSi plane, the observed lower intensity ratios for $\alpha = 1.0, 1.37,$ and 1.84 compared with that for $\alpha = 0.72$ were reproduced by the calculation, indicating that the proposed SSFU compositions are basically valid regarding the order between the nominal Mn site and the nominal Si site. In more detail, the experimental $I(111)/I(022)$ decreased with α increasing from 0.72 to 1.0 , in agreement with the calculation. In contrast, the experimental $I(111)/I(022)$ increased with α increasing from 1.0 to 1.37 and 1.84 , which is in disagreement with the calculation. To identify the possible origin of this increase, we should note that the experimental μ_s for $\text{Co}_2\text{Mn}_\alpha\text{Si}_{0.88}$ films showed a distinct decrease with α increasing beyond 1.53 , as will be shown in Fig. 6(a) in Sec. III B and that the TMR ratio at 290 K for CMS MTJs having $\beta = 0.88$ CMS electrodes showed a decrease with α increasing beyond 1.48 , as will be discussed in Sec. III C. Furthermore, the decrease in μ_s and the TMR ratio for α larger than a certain critical value, α_c , was also observed for other β series. These decreases in the experimental μ_s and TMR ratios with increasing $\alpha > \alpha_c$ can be explained by the appearance of a second phase that is a nonmagnetic or antiferromagnetic material and is not a half-metal. One possible candidate for the second phase is antiferromagnetic Mn_3Si with a Néel temperature of 25 K [44]. Furthermore, Mn_3Si is theoretically predicted not to be a half-metal [45]. Thus, the assumption of the appearance of Mn_3Si as the second phase can explain the decrease in the experimental μ_s and TMR ratios with increasing $\alpha > \alpha_c$. Regarding the structural properties, Mn_3Si crystallizes in a DO_3 structure having lattice constant $a = 0.5722$ nm [44], which is close to the values for CMS films (Tables I and II), and its crystal structure has the same basic unit cell as the $L2_1$ structure of Heusler alloy CMS.

If Mn_3Si appeared as the second phase, the SSFU composition of the CMS matrix would shift to a reduced Mn composition with respect to Co and Si. The occupation of Si at the nominal site, γ_2 , would thus increase in the CMS matrix, resulting in an increase in the 111 peak intensity. Since the $\alpha = 1.84$ film ($\text{Co}_2\text{Mn}_{1.84}\text{Si}_{0.88}$) is obviously in the range of $\alpha > \alpha_c$, the increase in the experimental $I(111)/I(022)$ and the decrease in the experimental μ_s for the $\alpha = 1.84$ film of the $\beta = 0.88$ CMS film series can be consistently explained. To sum up, although we could not get a full understanding of the origin of the increase in the experimental $I(111)/I(022)$ for $\alpha = 1.37$ and 1.84 , we propose that Mn_3Si , which is antiferromagnetic and not half-metallic, appears as a second phase, to explain the increased $I(111)/I(022)$ for $\alpha = 1.84$.

To further characterize the structural properties, we directly observed lattice images of Mn-deficient and Mn-rich CMS films at atomic resolution using aberration-corrected Z-contrast STEM. Figures 5(a) and 5(b) show typical Z-contrast STEM images for a Mn-deficient $\text{Co}_2\text{Mn}_{0.72}\text{Si}_{0.88}$ film (SSFU composition $\text{Co}_2[\text{Mn}_{0.78}\text{Co}_{0.22}][\text{Si}_{0.98}\text{Mn}_{0.02}]$) and a Mn-rich $\text{Co}_2\text{Mn}_{1.37}\text{Si}_{0.88}$ film ($[\text{Co}_{1.88}\text{Mn}_{0.12}]\text{Mn}[\text{Si}_{0.83}\text{Mn}_{0.17}]$). The atomic lattice with all three sites is clearly visible. For the Mn-deficient film with $\alpha = 0.72$, almost all the observed area of $\sim 16 \times 14$ nm² had the $L2_1$ structure. Figure 5(c) shows an enlarged image of a region of Fig. 5(a), clearly showing the $L2_1$ structure. On the other hand, for the Mn-rich

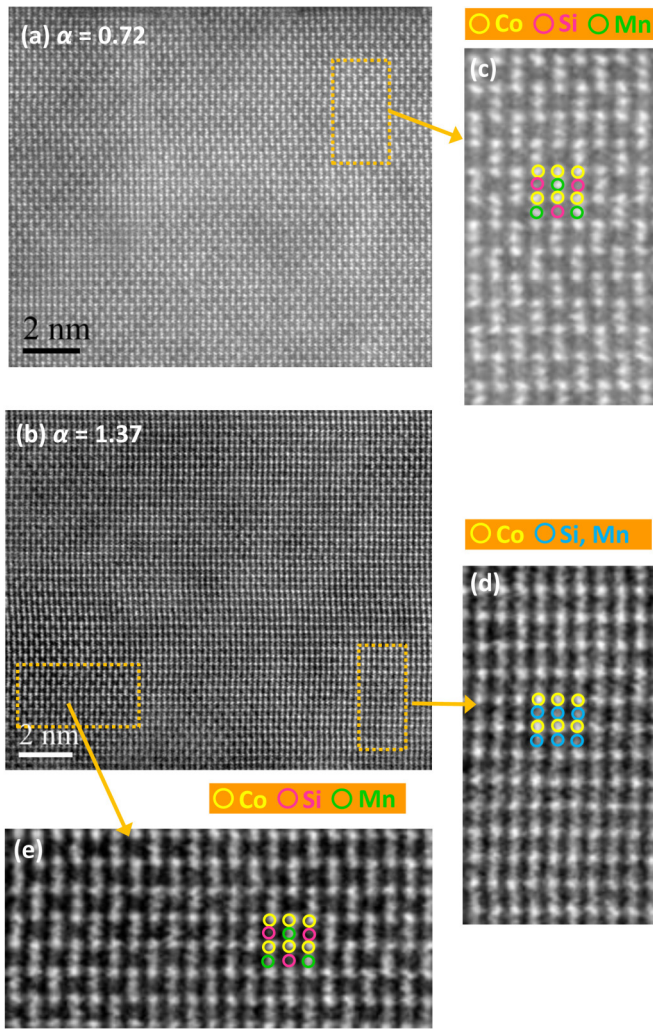


FIG. 5. (Color online) High-resolution Z-contrast scanning TEM (STEM) images of (a) a Mn-deficient $\text{Co}_2\text{Mn}_{0.72}\text{Si}_{0.88}$ film ($\alpha = 0.72$ in $\text{Co}_2\text{Mn}_\alpha\text{Si}_{0.88}$) and (b) a Mn-rich $\text{Co}_2\text{Mn}_{1.37}\text{Si}_{0.88}$ film ($\alpha = 1.37$), both with the area of $\sim 16 \times 14 \text{ nm}^2$. (c) Enlarged image of a region of (a) showing the $L2_1$ structure. (d) and (e) Enlarged images of two different regions of (b) showing the $B2$ and $L2_1$ structures, respectively.

film with $\alpha = 1.37$, a typical image with the same area consisted of mostly the $B2$ structure with small $L2_1$ regions. Figures 5(d) and 5(e) show enlarged images of two different regions of Fig. 5(b); they reveal $B2$ and $L2_1$ structures, respectively. STEM images for a Mn-rich $\text{Co}_2\text{Mn}_{1.32}\text{Si}_{0.88}$ film ($[\text{Co}_{1.90}\text{Mn}_{0.10}]\text{Mn}[\text{Si}_{0.84}\text{Mn}_{0.16}]$) showed a similar dominant $B2$ structure with small $L2_1$ regions as the Mn-rich $\text{Co}_2\text{Mn}_{1.37}\text{Si}_{0.88}$ film.

The dominant $L2_1$ structure region observed for the Mn-deficient film having $\alpha = 0.72$ and the decreased region of the $L2_1$ structure along with the dominant region of the $B2$ structure for the Mn-rich film having $\alpha = 1.37$ are in good agreement with the XRD findings. The decrease in the $L2_1$ area observed by Z-contrast STEM for the Mn-rich film ($\alpha = 1.37$) compared with that for the Mn-deficient film ($\alpha = 0.72$) agrees with the decreased XRD $I(111)/I(022)$ for the film with $\alpha = 1.37$ compared with the film with $\alpha = 0.72$. These features

are consistent with the lower Si occupation ratio at the nominal Si site in the proposed SSFU composition for the Mn-rich film with $\alpha = 1.37$ relative to that for the Mn-deficient film with $\alpha = 0.72$.

In summary, the experimental findings regarding the structural properties observed for both the XRD intensity ratios and HRSTEM images support the proposed SSFU compositions.

B. Saturation magnetization per formula unit composition

We now describe how the experimental saturation magnetization per formula μ_s of nonstoichiometric $\text{Co}_2\text{Mn}_\alpha\text{Si}_\beta$ ($\beta = 0.88$ and 1.0) films varied with α . We will compare the experimental μ_s with the theoretically calculated total spin magnetic moments per formula unit, m_{spin} , and with the Slater-Pauling rule for half-metallic Co_2YZ alloys, $Z_t - 24$ ($\mu_B/\text{f.u.}$) [23], where Z_t is the total number of valence electrons per formula unit provided by the SSFU composition and μ_B is the Bohr magneton. Figure 6(a) plots μ_s at 10 K and m_{spin} for $\text{Co}_2\text{Mn}_\alpha\text{Si}_{0.88}$ films with α ranging from 0.72 (Mn-deficient CMS) to 1.84 (Mn-rich CMS), while Fig. 6(b) compares m_{spin} with $Z_t - 24$. As shown in Fig. 6(a), μ_s is in good agreement with m_{spin} over a wide range of α from 0.72 to 1.37. For a strongly Mn-deficient composition ($\alpha = 0.72$), μ_s was markedly lower than $Z_t - 24$. However, μ_s increased with an increase in α over $\alpha = 0.72$, growing closer to $Z_t - 24$ and was very close to $Z_t - 24$ for $\alpha = 1.15$ to 1.37. The μ_s was appreciably lower than m_{spin} for $\alpha = 1.53$, and it decreased significantly with a further increase in α . We estimated the critical value α_c over which μ_s decreased to be $\alpha_c = 1.53$ for $\beta = 0.88$, midway between 1.37 and 1.68.

As shown in Fig. 6(b), m_{spin} for $\alpha = 0.72$ was distinctly lower than the half-metallic value, $Z_t - 24$. However, m_{spin} increased with increasing α , growing closer to $Z_t - 24$. Note that the Co atomic ratio at the nominal Mn site decreased with α increasing from 0.72 in accordance with the SSFU composition model (Table II). The two values are in good agreement for $\alpha = 1.15$ ($[\text{Co}_{1.99}\text{Mn}_{0.01}]\text{Mn}[\text{Si}_{0.88}\text{Mn}_{0.12}]$) to 1.84 ($[\text{Co}_{1.69}\text{Mn}_{0.31}]\text{Mn}[\text{Si}_{0.75}\text{Mn}_{0.25}]$, where the CoMn antisites are suppressed.

To confirm the reproducibility of these features for the α dependence of μ_s , we also investigated μ_s values for the $\beta = 1.0$ film series ($\text{Co}_2\text{Mn}_\alpha\text{Si}_{1.0}$). Figure 6(c) plots μ_s at 10 K and m_{spin} for $\text{Co}_2\text{Mn}_\alpha\text{Si}_{1.0}$ films with α ranging from 0.69 to 1.44, while Fig. 6(d) compares m_{spin} with $Z_t - 24$. As shown in Fig. 6(c), the dependence of μ_s on α was well reproduced by m_{spin} for a wide range of α from 0.69 to 1.29, although we observed a small scattering of μ_s for $\beta = 1.0$ as a function of α for $\alpha = 0.85$ to 1.29. This small scattering of μ_s was probably due to experimental errors and not to an intrinsic factor because common features for the α dependence of μ_s were observed for both $\beta = 0.88$ and 1.0 and because a more continuous change in μ_s with respect to α was observed for $\beta = 0.88$. For a strongly Mn-deficient composition ($\alpha = 0.69$), μ_s was markedly lower than $Z_t - 24$. However, μ_s increased with an increase in α over $\alpha = 0.69$ and was close to $Z_t - 24$ for $\alpha = 1.0$ to 1.29. With an even further increase in α , μ_s decreased significantly. Thus, the characteristic dependence of μ_s on α observed in the $\beta = 0.88$ films was also observed in the $\beta = 1.0$ films. As shown in Fig. 6(d), the dependence of m_{spin} on

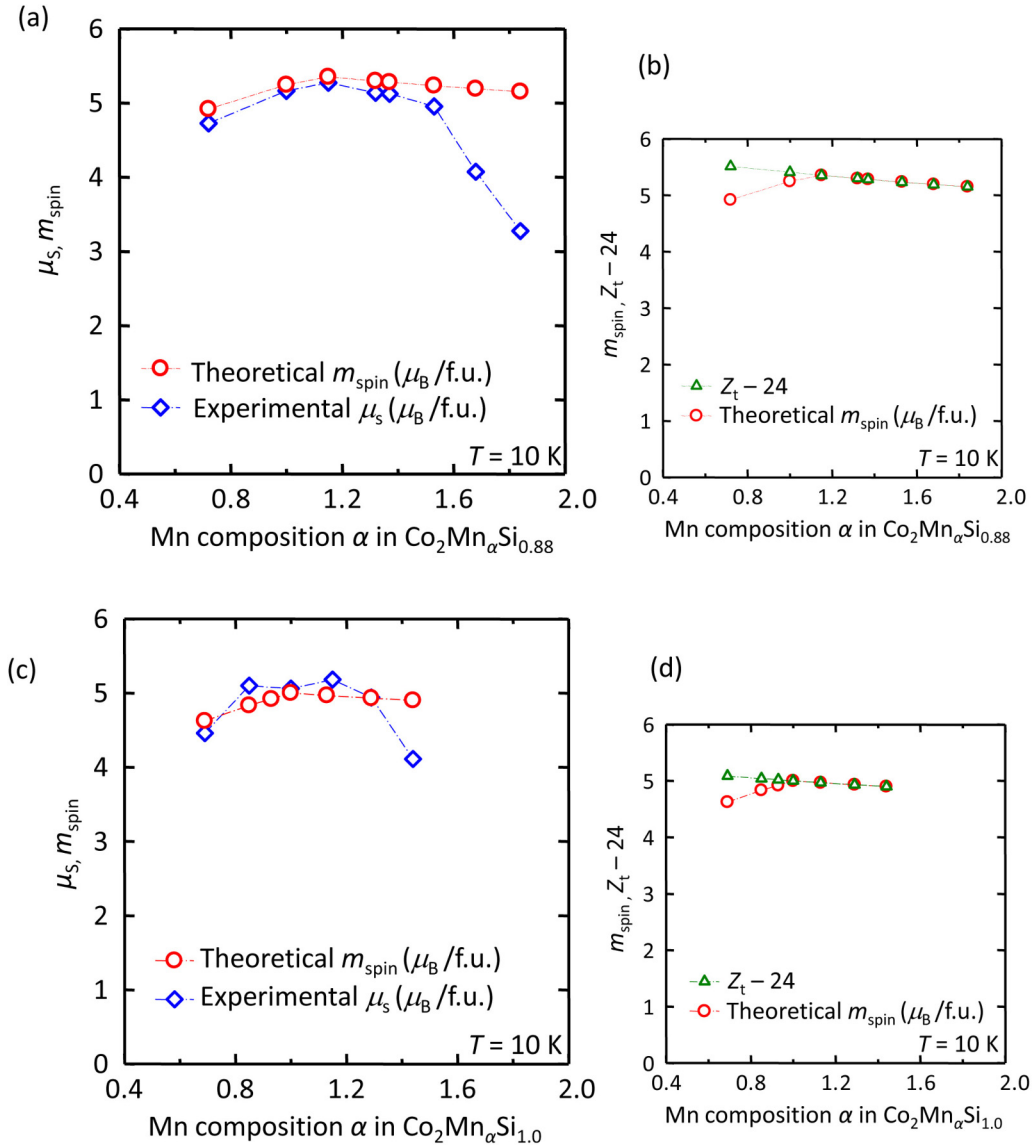


FIG. 6. (Color online) (a) Experimental μ_s values at 10 K and theoretical m_{spin} values obtained by KKR-CPA calculations as a function of α for $\text{Co}_2\text{Mn}_\alpha\text{Si}_{0.88}$. (b) Theoretical m_{spin} values and $Z_t - 24$, where Z_t is the total valence electron number/formula unit provided by the SSFU compositions as a function of α for $\text{Co}_2\text{Mn}_\alpha\text{Si}_{0.88}$. (c) Experimental μ_s values at 10 K and theoretical m_{spin} values as a function of α for $\text{Co}_2\text{Mn}_\alpha\text{Si}_{1.0}$. (d) Theoretical m_{spin} values and $Z_t - 24$ as a function of α for $\text{Co}_2\text{Mn}_\alpha\text{Si}_{1.0}$.

α for $\beta = 1.0$ was similar to that for $\beta = 0.88$. The m_{spin} for $\alpha = 0.69$ was distinctly lower than $Z_t - 24$ [Fig. 6(d)], but m_{spin} increased with increasing α , growing closer to $Z_t - 24$. The two values are in good agreement for $\alpha = 1.0$ to 1.44 .

There was good agreement between μ_s and $Z_t - 24$ for $\alpha = 1.15$ to 1.37 for $\text{Co}_2\text{Mn}_\alpha\text{Si}_{0.88}$ films, as shown in Figs. 6(a) and 6(b), and for $\alpha = 1.0$ to 1.29 for $\text{Co}_2\text{Mn}_\alpha\text{Si}_{1.0}$ films, as shown in Figs. 6(c) and 6(d). These observations indicate that $\text{Co}_2\text{Mn}_\alpha\text{Si}_{0.88}$ films with α ranging from 1.15 to 1.37 and $\text{Co}_2\text{Mn}_\alpha\text{Si}_{1.0}$ films with α ranging from 1.0 to 1.29 are close to half-metals.

To clarify the origin of the decrease in μ_s with respect to $Z_t - 24$ for Mn-deficient CMS films (Mn deficiency generally corresponds to $\alpha < 2 - \beta$ for the expression of $\text{Co}_2\text{Mn}_\alpha\text{Si}_\beta$), we calculated by KKR-CPA the α dependence of the Co and Mn spin magnetic moments, $m_{\text{spin}}(\text{Co})$ and $m_{\text{spin}}(\text{Mn})$, at the

respective regular site and antisite. The calculated $m_{\text{spin}}(\text{Co})$ and $m_{\text{spin}}(\text{Mn})$ are shown for $\text{Co}_2\text{Mn}_\alpha\text{Si}_{0.88}$ films in Figs. 7(a) and 7(b). In Fig. 7, the KKR-CPA calculations indicate that the spin magnetic moment of Co at the nominal Mn site, $m_{\text{spin}}(\text{Co}_{\text{Mn}})$, is much smaller than that of Mn at the nominal Mn site, $m_{\text{spin}}(\text{Mn}_{\text{Mn}})$ ($m_{\text{spin}}(\text{Co}_{\text{Mn}}) = 1.89 \mu_B$ in contrast to $m_{\text{spin}}(\text{Mn}_{\text{Mn}}) = 3.29 \mu_B$ for $\alpha = 0.72$). This results in μ_s being lower than $Z_t - 24$ with decreasing $\alpha < 2 - \beta$. Thus, the loss of the half-metallicity in Mn-deficient CMS films, shown by μ_s being lower than $Z_t - 24$, originates from the Co_{Mn} antisite defects.

The good agreement between the experimental μ_s and theoretical m_{spin} values for both $\text{Co}_2\text{Mn}_\alpha\text{Si}_{0.88}$ films with $\alpha = 0.72$ to 1.37 and $\text{Co}_2\text{Mn}_\alpha\text{Si}_{1.0}$ films with $\alpha = 0.69$ to 1.29 supports the validity of the SSFU composition model based on the formation of antisites rather than

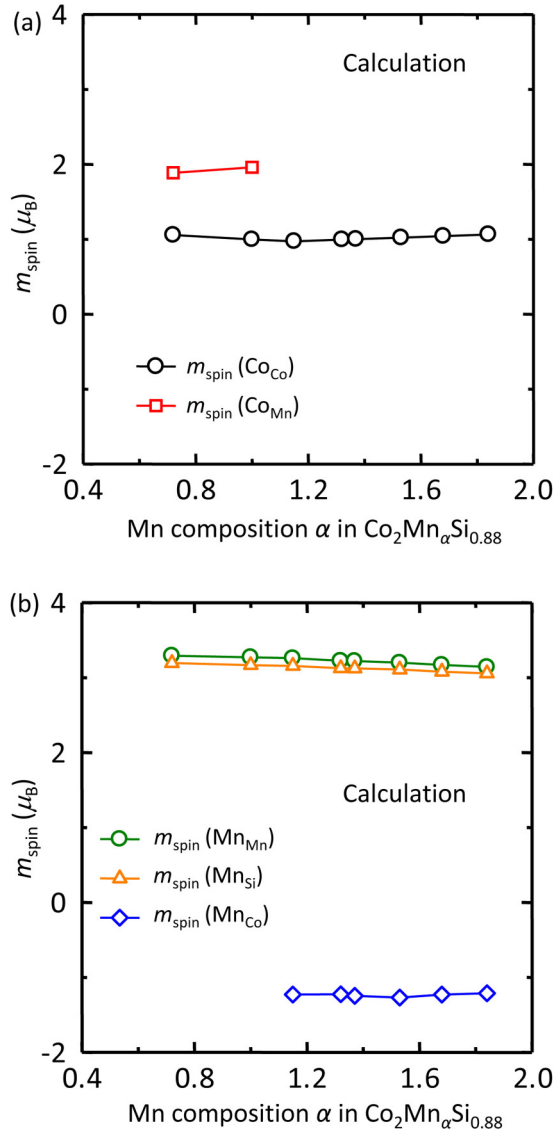


FIG. 7. (Color online) Mn composition dependence of (a) the Co spin magnetic moment and (b) Mn spin magnetic moment at different sites deduced from the KKR-CPA calculations for $\text{Co}_2\text{Mn}_\alpha\text{Si}_{0.88}$.

the formation of vacancies as a good approximation for nonstoichiometric $\text{Co}_2\text{Mn}_\alpha\text{Si}_\beta$ with α of up to a certain Mn-rich composition.

A significant drop in the saturation magnetization per formula unit from m_{spin} with α increasing beyond α_c was observed for both $\beta = 0.88$ and 1.0 . We estimated α_c for $\beta = 1.0$ to be $\alpha_c = 1.37$, which is midway between 1.29 and 1.44 . Thus, we obtained α_c values of 1.53 and 1.37 for $\beta = 0.88$ and 1.0 , respectively. Note that α_c increased for β decreasing from 1.0 (larger Si deficiency). This behavior of μ_s for $\alpha > \alpha_c$ can be explained by the appearance of a second phase that is nonmagnetic or antiferromagnetic. Mn_3Si is a tentative candidate for the second phase, as discussed in Sec. III A.

C. TMR ratio

In this section, we first summarize the experimental α dependence of the TMR ratio of CMS MTJs having $\text{Co}_2\text{Mn}_\alpha\text{Si}_\beta$

electrodes, including the MgO-buffered $\beta = 1.0$ MTJs [8] and CoFe-buffered $\beta = 0.96$ MTJs [10], previously reported, and the CoFe-buffered $\beta = 0.88$ MTJs investigated in this study. Then, we theoretically investigate the α dependence of the spin polarization by using KKR-CPA calculations based on the SSFU composition model. We show that the α dependence of the theoretical spin polarization, $P_{\text{th}}(\text{spd})$, for Mn-deficient compositions in $\text{Co}_2\text{Mn}_\alpha\text{Si}_\beta$ electrodes differs significantly from that of $P_{\text{th}}(\text{sp})$, where $P_{\text{th}}(\text{spd})$ is determined by considering all the contributions from s -, p -, and d -like electrons for the majority- and minority-spin density of states (DOS) at E_F and where $P_{\text{th}}(\text{sp})$ is determined by considering only the contributions from s - and p -like electrons. By comparing the α dependence of the TMR ratio with that of $P_{\text{th}}(\text{spd})$ and $P_{\text{th}}(\text{sp})$, we show that the α dependence of the TMR ratio can be qualitatively explained by $P_{\text{th}}(\text{sp})$ for an α range from a Mn-deficient composition to a critical Mn-rich composition, α_c . Then, we show that the decrease in $P_{\text{th}}(\text{sp})$ with decreasing α in the Mn-deficient compositions is caused by a small amount of itinerant s - and p -orbital components of the local density of minority-spin in-gap states at E_F of Co at the nominal Mn site (Co_{Mn}) and at the regular site (Co_{Co}). We also show that α_c increases with decreasing β , suggesting a correlation between α_c and the SSFU composition.

Figures 8(a) and 8(b) show the TMR ratios at 290 and 4.2 K of CMS MTJs having $\text{Co}_2\text{Mn}_\alpha\text{Si}_\beta$ electrodes as a function of α for $\beta = 0.88, 0.96$, and 1.0 . The data for $\beta = 0.96$ and 1.0 MTJs were previously presented [10,8]. The $\beta = 0.88$ and 0.96 MTJs were prepared on CoFe-buffered MgO(001) substrates, but the $\beta = 1.0$ MTJs were prepared on MgO-buffered MgO(001). The TMR ratios of the CoFe-buffered $\beta = 0.88$ and 0.96 MTJs were significantly higher than those of the MgO-buffered $\beta = 1.0$ MTJs as a result of the enhanced coherent tunneling caused by the increased misfit dislocation spacing at the lower and upper MgO barrier interfaces [10]. Although the TMR ratios of CoFe-buffered CMS MTJs were much higher than those of MgO-buffered CMS MTJs, the dependences of their TMR ratios at 4.2 and 290 K on α were almost identical. In all three cases, the TMR ratio for the CMS MTJ series significantly increased with α increasing from a Mn-deficient composition up to a certain Mn-rich composition, α_c , beyond which it decreased.

For each CMS MTJ series, we estimated α_c as the value midway between the α for the maximum TMR ratio at 290 K and the next α . The α_c values for $\beta = 1.0, 0.96$, and 0.88 were $1.34, 1.42$, and 1.48 , respectively, which are the same as those determined from the TMR ratio at 4.2 K. The α_c values from the TMR ratio are, thus, in good agreement with those from μ_s (Sec. III B).

The α_c value increased with decreasing $\beta < 1.0$ (larger Si deficiency). This suggests a correlation between α_c and the SSFU compositions. The SSFU compositions were type III, $[\text{Co}_{2-x}\text{Mn}_x]\text{Mn}[\text{Si}_{1-y}\text{Mn}_y]$, for $\alpha \approx \alpha_c$. If we determine the critical values of x for the type III SSFU compositions, x_c , from α_c by following Table III, we obtain an almost identical value, $x_c = 0.17 \pm 3\%$, for $\beta = 1.0, 0.96$, and 0.88 . This suggests that there is an upper limit for Mn at Co sites. We suspect that films having $\alpha > \alpha_c$ contain a second phase that is nonmagnetic or antiferromagnetic and is not half-metallic, thereby explaining the decrease in μ_s and the TMR ratio for

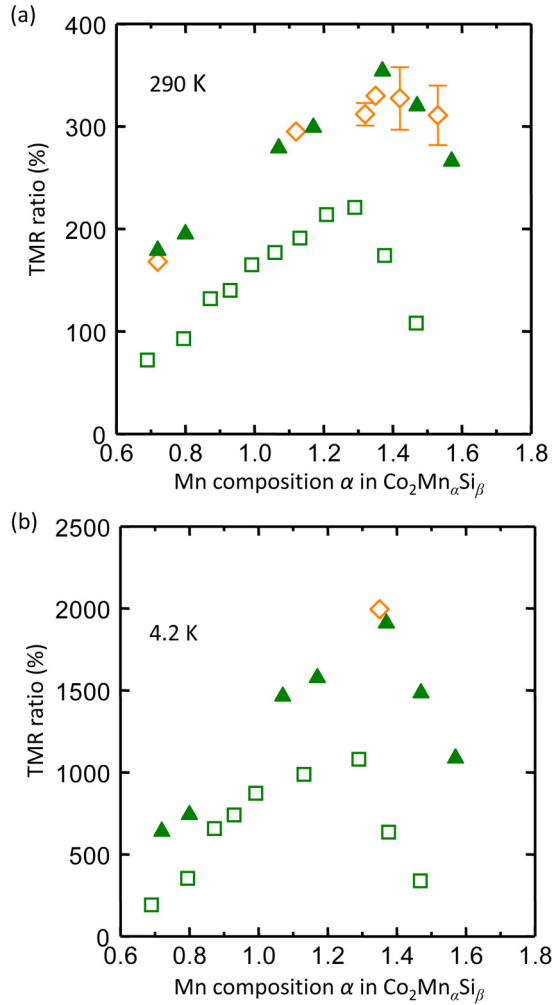


FIG. 8. (Color online) Mn composition dependence of the TMR ratios at (a) 290 K and (b) 4.2 K obtained for three series of $\text{Co}_2\text{Mn}_\alpha\text{Si}_\beta/\text{MgO}/\text{Co}_2\text{Mn}_\alpha\text{Si}_\beta$ MTJs (CMS MTJs) as a function of α , including MgO-buffered MTJs with $\text{Co}_2\text{Mn}_\alpha\text{Si}_{1.0}$ electrodes [9] (open rectangles), CoFe-buffered MTJs with $\text{Co}_2\text{Mn}_\alpha\text{Si}_{0.96}$ electrodes [10] (solid triangles), and CoFe-buffered MTJs with $\text{Co}_2\text{Mn}_\alpha\text{Si}_{0.88}$ electrodes (open diamonds).

$\alpha > \alpha_c$. One possible candidate for the second phase is Mn_3Si , as discussed in Sec. III A.

Figure 9 shows two kinds of theoretical spin polarization, $P_{\text{th}}(spd)$ and $P_{\text{th}}(sp)$, calculated for $\text{Co}_2\text{Mn}_\alpha\text{Si}_{1.0}$ for various α values ranging from $\alpha = 0.69$ to 1.44. The $P_{\text{th}}(spd)$ value was determined by considering all the contributions from s -, p -, and d -like electrons for the majority- and minority-spin DOS at E_F , $D_M(spd)$ and $D_m(spd)$, respectively. It is defined as

$$P_{\text{th}}(spd) = \frac{D_M(spd) - D_m(spd)}{D_M(spd) + D_m(spd)}. \quad (1)$$

The $P_{\text{th}}(sp)$ value was determined by considering only the contributions from s - and p -like electrons for the majority- and minority-spin DOS at E_F , $D_M(sp)$ and $D_m(sp)$, respectively. It is defined as

$$P_{\text{th}}(sp) = \frac{D_M(sp) - D_m(sp)}{D_M(sp) + D_m(sp)}. \quad (2)$$

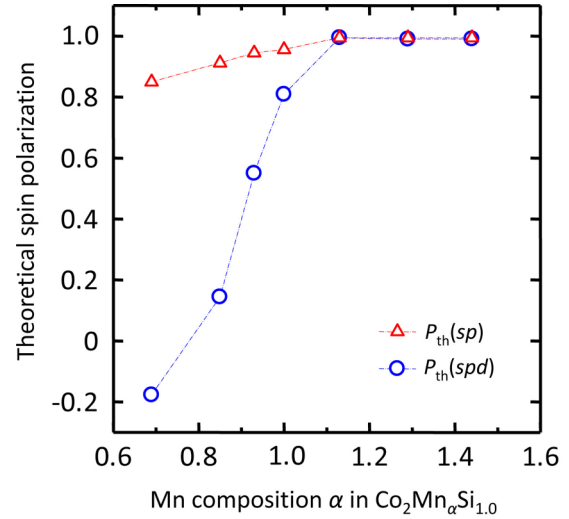


FIG. 9. (Color online) Two kinds of theoretical spin polarization, $P_{\text{th}}(spd)$, (open circles) and $P_{\text{th}}(sp)$, (open triangles) obtained by the KKR-CPA calculations as a function of α for $\text{Co}_2\text{Mn}_\alpha\text{Si}_{1.0}$ with $\alpha = 0.69$ to 1.44. The values for $P_{\text{th}}(spd)$ (0.81) and $P_{\text{th}}(sp)$ (0.96) for $\alpha = 1.0$ (stoichiometric CMS) were lower than 1.0, the value for half-metals, due to the atomic sphere approximation in the KKR-CPA calculation, which assumes a spherically symmetric potential in each atomic sphere. First-principles calculations performed using a full potential method showed half-metallicity for stoichiometric CMS [31,32].

As shown in Fig. 9, the values for $P_{\text{th}}(sp)$ and $P_{\text{th}}(spd)$ for $\text{Co}_2\text{Mn}_\alpha\text{Si}_{1.0}$ with $\alpha \geq 1.13$ were almost half-metallic: $P_{\text{th}}(sp) = 0.995$ and $P_{\text{th}}(spd) \geq 0.99$. The values for $P_{\text{th}}(spd)$ (0.81) and $P_{\text{th}}(sp)$ (0.96) for $\alpha = 1.0$ (stoichiometric CMS) were lower than 1.0, the value for half-metals, due to the atomic sphere approximation in the KKR-CPA calculation, which assumes a spherically symmetric potential in each atomic sphere. First-principles calculations performed using a full potential method, such as the ultrasoft pseudopotential method [31] or the full-potential linearized augmented plane-wave method [32], showed half-metallicity for stoichiometric CMS.

Note that the α dependence of $P_{\text{th}}(spd)$ for the Mn-deficient region differed markedly from that of $P_{\text{th}}(sp)$. $P_{\text{th}}(spd)$ decreased pronouncedly with α for $\alpha < 1.0$ and became negative for a strongly Mn-deficient composition ($\alpha = 0.69$). If the tunneling current in CMS MTJs was dominantly determined by $P_{\text{th}}(spd)$, the TMR ratio for $\alpha < 1.0$ would significantly decrease with α , become almost zero one time for $P_{\text{th}}(spd) \sim 0$, and then increase again to a certain positive value. However, the α dependence of the TMR ratio showed a monotonic decrease with α for $\alpha < 1.0$, in obvious disagreement with the α dependence of $P_{\text{th}}(spd)$. On the other hand, $P_{\text{th}}(sp)$ for $\alpha < 1.0$ was positive and increased with α from $P_{\text{th}}(sp) = 0.850$ for $\alpha = 0.69$ to 0.945 for $\alpha = 0.93$. Thus, the α dependence of $P_{\text{th}}(sp)$, in contrast to that of $P_{\text{th}}(spd)$, was found to qualitatively explain the α dependence of the TMR ratio except for $\alpha > \alpha_c$. This suggests that tunneling in CMS/MgO-based MTJs is mainly due to itinerant s - and p -like electrons and the contribution to tunneling from localized d -like electrons is negligible. This picture is essentially the same as the one

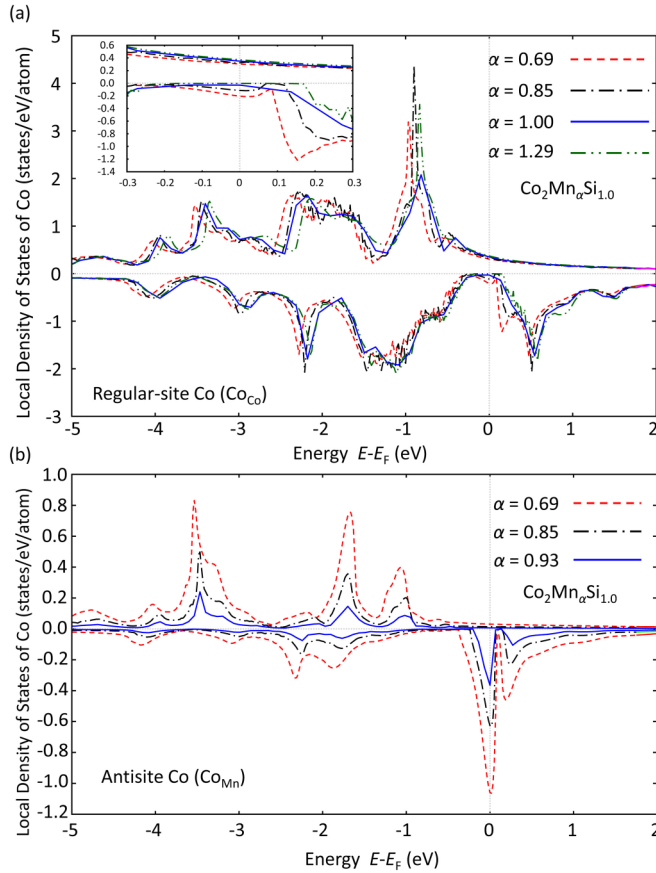


FIG. 10. (Color online) LDOS for (a) Co at the regular site (Co_{Co}) and (b) Co at the nominal Mn site (Co_{Mn}) for $\text{Co}_2\text{Mn}_\alpha\text{Si}_{1.0}$ for various α as a function of energy E relative to the Fermi level (E_F). Inset shows a magnification of the LDOS of the nominal site Co near E_F . Majority spin states are shown as positive LDOS and minority spin states as negative.

proposed for the tunneling spin polarizations of ferromagnetic transition metals by Stearns [46]. In principle, the contribution from the delocalized $d(3z^2-r^2)$ orbital component involved in the majority-spin Δ_1 symmetry should be included in the theoretical tunneling spin polarization, which is equivalent to $P_{\text{th}}(sp)$ in the discussion above. However, it can be neglected because the contributions from s and $p(z)$ orbitals are dominant.

Figures 10(a) and 10(b), respectively, show how the LDOS of Co at the regular site (Co_{Co}) and at the nominal Mn site (Co_{Mn}) of $\text{Co}_2\text{Mn}_\alpha\text{Si}_{1.0}$ depended on α , which can help us understand the decrease in the spin polarization of Mn-deficient CMS films. Figure 10(b) shows the appearance of minority-spin in-gap states around E_F for the antisite Co (Co_{Mn}). It also shows that the density of the minority-spin in-gap states around E_F for Co_{Mn} increased for the more strongly Mn-deficient $\text{Co}_2\text{Mn}_\alpha\text{Si}_{1.0}$. Furthermore, Co_{Mn} antisites for Mn-deficient CMS affected the electronic state of Co atoms at the regular sites, resulting in the appearance of minority-spin in-gap states around E_F for Co_{Co} although the minority-spin LDOS around E_F for Co_{Co} was smaller than that for Co_{Mn} . These minority-spin in-gap states around E_F for both antisite Co_{Mn} and regular-site Co_{Co} were mainly composed of

localized $\text{Co}-d(x^2-y^2)$ orbital components along with a small amount of itinerant s - and $p(z)$ orbital components. Then, the decrease in $P_{\text{th}}(sp)$ from the half-metallic value of 1.0 for Mn-deficient $\text{Co}_2\text{Mn}_\alpha\text{Si}_{1.0}$ is ascribed to the s - and $p(z)$ orbital components of the local density of minority-spin in-gap states at E_F of Co_{Mn} and Co_{Co} . The Co_{Mn} and Co_{Co} components affect $P_{\text{th}}(sp)$ to the same degree, leading to a decrease in $P_{\text{th}}(sp)$ from 1.0. This is because the number of Co_{Co} in the formula unit for $\alpha < 1.0$ [for example, 2 for $\alpha = 0.69$ (Table I)] is much larger than that of Co_{Mn} (0.17 for $\alpha = 0.69$), while the local density of minority-spin in-gap states at E_F for Co_{Mn} is several times larger than that for Co_{Co} .

In contrast, the minority-spin LDOS around E_F for Mn at the regular site (Mn_{Mn}), at the Si site (Mn_{Si} antisite), and at the Co site (Mn_{Co} antisite) for $\text{Co}_2\text{Mn}_\alpha\text{Si}_{1.0}$ for various values of α was negligibly small (not shown). This is consistent with previous theoretical results: half-metallicity is retained for the existence of a single Mn_{Co} antisite [33] and is robust for disorder between Mn and Si in $\text{Co}_2\text{Mn}_{1-x}\text{Si}_{1+x}$ and $\text{Co}_2\text{Mn}_{1-x}\text{Si}_{1+x}$ [35].

In our SSFU composition model, Co_{Mn} antisites are not present in $\text{Co}_2\text{Mn}_\alpha\text{Si}_\beta$ for $\alpha \geq 2 - \beta$. The KKR-CPA calculations for this composition range showed half-metallicity due to the disappearance of the minority-spin in-gap states around E_F . Picozzi *et al.* [33] theoretically predicted that a single Co_{Mn} antisite produces minority-spin states at E_F and thus degrades for the half-metallicity of Co_2MnZ ($Z = \text{Si}$ and Ge). Our KKR-CPA calculations demonstrated that this picture is generally valid for strongly Mn-deficient CMS and revealed increasing minority-spin DOS around E_F for more strongly Mn-deficient $\text{Co}_2\text{Mn}_\alpha\text{Si}_{1.0}$.

Next, we describe the correlation of the degree of T dependence of the TMR ratio with the Mn composition α in $\text{Co}_2\text{Mn}_\alpha\text{Si}_\beta$ electrodes. If we use parameter $\gamma = \text{TMR}(4.2 \text{ K})/\text{TMR}(290 \text{ K})$ to represent the degree of T dependence of the TMR ratio, the γ values for the CMS MTJs were higher than those for $\text{CoFeB}/\text{MgO}/\text{CoFeB}$ MTJs. For example, the γ value for the CoFe-buffered CMS MTJ with $\alpha = 1.37$ in $\text{Co}_2\text{Mn}_\alpha\text{Si}_{0.96}$ electrodes, which showed TMR ratios of 1910% at 4.2 K and 354% at 290 K [10], was 5.4, which is much larger than the 2.0 reported for a $\text{CoFeB}/\text{MgO}/\text{CoFeB}$ MTJ, which showed TMR ratios of 1144% at 5 K and 576% at 300 K [47]. It is, however, beyond the scope of this paper to speculate on the origin of the strong T dependence of the TMR ratio of CMS MTJs, and it will be discussed in a subsequent report [48].

Here, we focus on the Mn composition dependence of γ for CMS MTJs. As a typical result, Fig. 11(a) plots γ for CoFe-buffered CMS MTJs having $\text{Co}_2\text{Mn}_\alpha\text{Si}_{0.96}$ electrodes as a function of α . The γ value increased with α up to $\alpha = 1.37$, from $\gamma = 3.6$ for $\alpha = 0.72$ (TMR ratio at 4.2 K = 640%) to $\gamma = 5.4$ for $\alpha = 1.37$ (TMR ratio at 4.2 K = 1910%). It subsequently decreased with a further increase in α beyond 1.37 accompanying the decrease in the TMR ratio at 4.2 K. We call the first region, from $\alpha = 0.72$ to 1.37, α -region I and the second one, $\alpha > 1.37$ (particularly including $\alpha = 1.47$ and 1.57), α -region II.

As shown previously for a CMS MTJ with Mn-deficient CMS electrodes [49], and as will be separately shown for CMS MTJs with various Mn compositions [50], $R_P (= 1/G_P)$ of these MTJs was mostly independent of T from

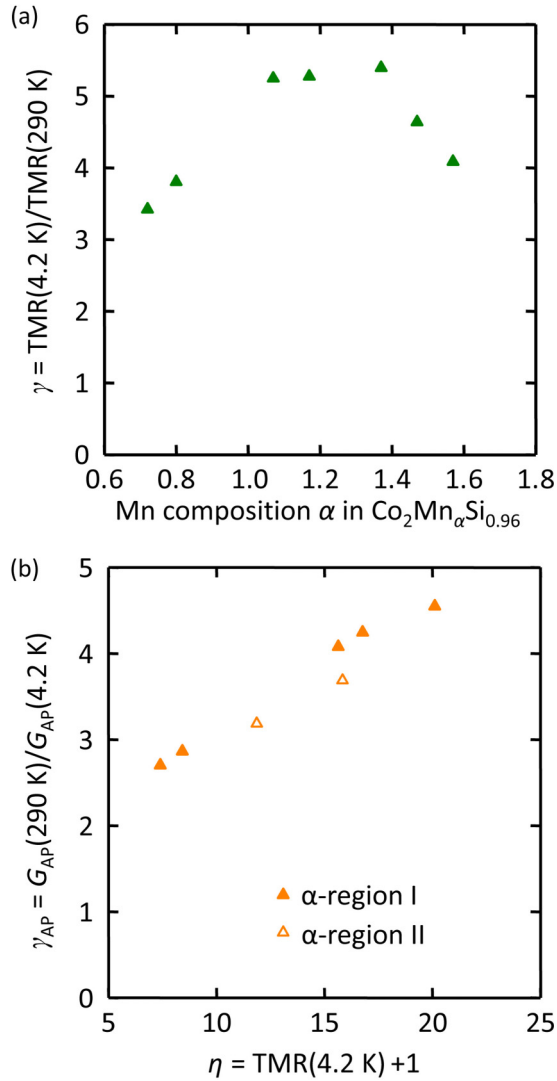


FIG. 11. (Color online) Dependence of parameter $\gamma = \text{TMR}(4.2 \text{ K})/\text{TMR}(290 \text{ K})$ on α (a) and that of parameter $\gamma_{\text{AP}} = G_{\text{AP}}(290 \text{ K})/G_{\text{AP}}(4.2 \text{ K})$ on $\eta = \text{TMR}(4.2 \text{ K}) + 1 \approx 1/\xi = (1+P^2)/(1-P^2)$ (b) for CMS/MgO/CMS MTJs having $\text{Co}_2\text{Mn}_\alpha\text{Si}_{0.96}$ electrodes, where TMR represents TMR ratio, P is the tunneling spin polarization at the Fermi level, and G_{AP} represents the tunneling conductance for the antiparallel configuration at a small dc voltage. In (b), γ_{AP} values for both α -region I (solid triangles) ranging from Mn-deficient $\alpha = 0.72$ ($\eta = 7.4$) to Mn-rich $\alpha = 1.37$ ($\eta = 20.1$) and α -region II (open triangles) $\alpha > 1.37$, particularly including $\alpha = 1.47$ ($\eta = 15.8$) and 1.57 ($\eta = 11.9$), are plotted.

4.2 K to RT, while $R_{\text{AP}} (= 1/G_{\text{AP}})$ was strongly dependent on T , resulting in the TMR ratio being mostly determined by that of R_{AP} , where G_{P} and G_{AP} are the respective tunneling conductances at a small dc voltage for the parallel and antiparallel configurations. Furthermore, as the TMR ratio at 4.2 K increased with α from Mn-deficient to Mn-rich, the degree of the T dependence of G_{AP} increased, i.e., parameter $\gamma_{\text{AP}} = G_{\text{AP}}(290 \text{ K})/G_{\text{AP}}(4.2 \text{ K})$ increased with α in α -region I. Note that γ_{AP} is closely related to $\gamma = \text{TMR}(4.2 \text{ K})/\text{TMR}(290 \text{ K})$ for CMS MTJs because the quantity $(\text{TMR}(4.2 \text{ K})+1)/(\text{TMR}(290 \text{ K})+1)$ can be approx-

imated by $G_{\text{AP}}(290 \text{ K})/G_{\text{AP}}(4.2 \text{ K}) = \gamma_{\text{AP}}$ for CMS MTJs given that the difference between $G_{\text{P}}(4.2 \text{ K})$ and $G_{\text{P}}(290 \text{ K})$ is negligible compared with the T dependence of G_{AP} . As will be separately reported [50], the T dependences of G_{AP} from 4.2 K to 290 K for MTJs with various α values were well fitted by the model of Zhang *et al.* [51], in which the increase in G_{AP} with increasing T is ascribed to inelastic tunneling associated with spin-flip scattering via a thermally excited magnon at finite temperatures. According to this model, the T dependence of G_{AP} is given by

$$\frac{G_{\text{AP}}(T)}{G_{\text{AP}}(T=0)} = \left\{ 1 + Q \frac{2S}{E_m} \frac{1}{\xi} k_B T \cdot f(T) \right\}, \quad (3)$$

$$f(T) = -\ln(1 - \exp(-E_c/k_B T)) \quad (f(T) > 0), \quad (4)$$

where $Q = 1/(|T^d|^2/|T^j|^2 + 2S^2)$, $\xi = 2D_M D_m/(D_M^2 + D_m^2) = (1 - P^2)/(1 + P^2)$, P is the tunneling spin polarization at E_F , and D_M and D_m are the majority-spin and minority-spin DOS at E_F , respectively. Other parameters, including T^d , T^j , S , E_m , and E_c , are given elsewhere [51]. The quantity $1/\xi$ is related to $G_{\text{P}}(T=0)$ and $G_{\text{AP}}(T=0)$ [51]:

$$\frac{1}{\xi} = \frac{G_{\text{P}}(T=0)}{G_{\text{AP}}(T=0)} = \text{TMR}(T=0) + 1. \quad (5)$$

Given that the $G_{\text{AP}}(T)$ values of the CoFe-buffered CMS MTJs were well fitted by Eq. (3) [50], we will discuss the behavior of γ_{AP} on the basis of the Zhang *et al.* model. Approximating $G_{\text{AP}}(4.2 \text{ K})$ in the expression $\gamma_{\text{AP}} = G_{\text{AP}}(290 \text{ K})/G_{\text{AP}}(4.2 \text{ K})$ by $G_{\text{AP}}(T=0)$ and $\text{TMR}(T=0)$ in Eq. (5) by $\text{TMR}(4.2 \text{ K})$, we obtain an approximate expression for γ_{AP} from Eq. (3):

$$\gamma_{\text{AP}} \approx \left\{ 1 + Q \frac{2S}{E_m} \eta \cdot k_B T \cdot f(T) \right\}_{T=290 \text{ K}}, \quad (6)$$

$$\frac{1}{\xi} \approx \text{TMR}(4.2 \text{ K}) + 1 = \eta. \quad (7)$$

Figure 11(b) plots γ_{AP} for the CoFe-buffered CMS MTJs having $\text{Co}_2\text{Mn}_\alpha\text{Si}_{0.96}$ electrodes as a function of $\eta = \text{TMR}(4.2 \text{ K}) + 1$, including α -regions I and II. It clearly shows that γ_{AP} increased almost linearly with η , particularly for α -region I, which means that the product of the coefficients $Q \cdot 2S/E_m$ and $f(290 \text{ K})$, where the latter includes a factor E_c , was almost independent of α for α -region I for the CoFe-buffered CMS MTJs and that $\eta \approx 1/\xi = (1 + P^2)/(1 - P^2)$ was a dominant factor determining γ_{AP} . Furthermore, the γ_{AP} values for both α -regions showed a similar linear dependence on η even though those of α -region II were slightly lower than the linear approximation of those of α -region I. The linear dependence of γ_{AP} on η , particularly for α -region I, suggests that the observed increase in the degree of T dependence of the TMR ratio represented by γ with α is an intrinsic property explained by the model of Zhang *et al.* Thus, we experimentally clarified that the degree of T dependence of the TMR ratio of CMS MTJs from 4.2 K to RT increased with an increase in the tunneling spin polarization or equivalently with that of the TMR ratio at 4.2 K. From a more qualitative point of view, the increase in γ_{AP} , with an increase in the tunneling spin polarization, is reasonable given that G_{AP} at 4.2 K decreases with a

decrease in D_m , while the increase in G_{AP} at finite temperatures from $G_{AP}(4.2\text{ K})$, δG_{AP} , is proportional to $D_M^2 + D_m^2$ ($\approx D_M^2$ for high spin polarizations), according to the Zhang *et al.* model [51]. A similar dependence of γ_{AP} on $\eta = \text{TMR}(4.2\text{ K})+1$ was found in MgO-buffered CMS MTJs [50].

The linear increase in γ_{AP} with $\eta \approx 1/\xi = (1+P^2)/(1-P^2)$ is also consistent with our understanding that the dominant factor leading to the increase in the TMR ratio with increasing α up to the respective Mn-rich α_c values for MgO-buffered and CoFe-buffered CMS MTJs is the increase in the tunneling spin polarization arising from the decrease in Co_{Mn} antisites. This means that although the coherent tunneling contribution for both MgO-buffered and CoFe-buffered CMS MTJs is evident and the degree of the contribution is significantly larger for the latter [10], the degree is mostly independent of α in $\text{Co}_2\text{Mn}_\alpha\text{Si}_\beta$ electrodes of the MgO-buffered CMS MTJs and the CoFe-buffered MTJs.

Finally, note that the TMR ratios at both 4.2 and 290 K still increased in the Mn-rich region defined by $\alpha > 2 - \beta$ of the $\text{Co}_2\text{Mn}_\alpha\text{Si}_\beta$ electrodes up to $\alpha = \alpha_c$ and that γ_{AP} for CMS MTJs having $\text{Co}_2\text{Mn}_\alpha\text{Si}_{0.96}$ electrodes also increased almost linearly with η with an increase in α in the Mn-rich region, $\alpha > 2 - \beta$, particularly for $\alpha = 1.17$ and 1.37. These results indicate that there is a slight difference between the Co_{Mn} antisite concentration of thin films prepared by sputtering and the nominal concentration given by the SSFU model and that the concentration in thin films was further reduced by an increase in α even in the Mn-rich region up to $\alpha = \alpha_c$.

IV. CONCLUSION

The effect of nonstoichiometry on the half-metallic character of Co_2MnSi (CMS) was experimentally investigated through the Mn composition (α) dependence of the saturation magnetization per formula unit (μ_s) of $\text{Co}_2\text{Mn}_\alpha\text{Si}_\beta$ thin films and the TMR ratio of CMS/MgO/CMS MTJs (CMS MTJs) having $\text{Co}_2\text{Mn}_\alpha\text{Si}_\beta$ electrodes with various values of α and

$\beta = 1.0, 0.96, \text{ or } 0.88$. Experimental μ_s and TMR ratios were compared with KKR-CPA calculations based on the SSFU composition model, which assumes the formation of only antisite defects, not vacancies, to accommodate nonstoichiometry. The α dependence of μ_s was in good agreement with the KKR-CPA results. In particular, the decrease in μ_s for Mn-deficient films was explained by the smaller spin magnetic moment of Co at the nominal Mn site (Co_{Mn}) in comparison with Mn at the nominal Mn site. The α dependence of the TMR ratio of CMS MTJs having $\text{Co}_2\text{Mn}_\alpha\text{Si}_\beta$ electrodes was qualitatively explained by the theoretical spin polarizations obtained from only the s - and p -orbital components of the DOS at E_F in the KKR-CPA results. It was shown that minority-spin in-gap states around E_F were induced for not only antisite Co_{Mn} atoms but also Co atoms at the regular sites (Co_{Co}) in Mn-deficient CMS films. The decrease in the TMR ratio observed for CMS MTJs having Mn-deficient electrodes was ascribed to small s - and p -orbital components of the local density of minority-spin in-gap states at E_F that appeared for both the antisite Co_{Mn} and regular-site Co_{Co} . In conclusion, these findings demonstrate the presence of harmful Co_{Mn} antisites in Mn-deficient CMS and the effectiveness of preparing CMS thin films with a Mn-rich composition to retain the half-metallic character of CMS.

ACKNOWLEDGMENTS

This work was partly supported by Grants-in-Aid for Scientific Research (Grants No. 23246055 and No. 25286039) from the Ministry of Education, Culture, Sports, Science, and Technology, Japan, and by the Japan Science and Technology Agency through its Strategic International Cooperative Program under the title Advanced Spintronic Materials and Transport Phenomena. Electron microscopy at the University of Wisconsin (P.M.V. and F.S.) was supported by the U.S. Department of Energy, Basic Energy Sciences (Grant No. DE-FG02-99ER45777).

-
- [1] I. Žutić, J. Fabian, and S. Das Sarma, *Rev. Mod. Phys.* **76**, 323 (2004).
 - [2] R. A. de Groot, F. M. Mueller, P. G. van Engen, and K. H. J. Buschow, *Phys. Rev. Lett.* **50**, 2024 (1983).
 - [3] C. Felser, G. H. Fecher, and B. Balke, *Angew. Chem., Int. Ed.* **46**, 668 (2007).
 - [4] K. Inomata, S. Okamura, R. Goto, and N. Tezuka, *Jpn. J. Appl. Phys.* **42**, L419 (2003).
 - [5] S. Kämmerer, A. Thomas, A. Hütten, and G. Reiss, *Appl. Phys. Lett.* **85**, 79 (2004).
 - [6] Y. Sakuraba, M. Hattori, M. Oogane, Y. Ando, H. Kato, A. Sakuma, and T. Miyazaki, and H. Kubota, *Appl. Phys. Lett.* **88**, 192508 (2006).
 - [7] T. Ishikawa, T. Marukame, H. Kijima, K.-i. Matsuda, T. Uemura, M. Arita, and M. Yamamoto, *Appl. Phys. Lett.* **89**, 192505 (2006).
 - [8] T. Ishikawa, H.-x. Liu, T. Taira, K.-i. Matsuda, T. Uemura, and M. Yamamoto, *Appl. Phys. Lett.* **95**, 232512 (2009).
 - [9] M. Yamamoto, T. Ishikawa, T. Taira, G.-f. Li, K.-i. Matsuda, and T. Uemura, *J. Phys.: Condens. Matter* **22**, 164212 (2010).
 - [10] H.-x. Liu, Y. Honda, T. Taira, K.-i. Matsuda, M. Arita, T. Uemura, and M. Yamamoto, *Appl. Phys. Lett.* **101**, 132418 (2012).
 - [11] H.-x. Liu, Y. Honda, K.-i. Matsuda, M. Arita, T. Uemura, and M. Yamamoto, *Jpn. J. Appl. Phys.* **51**, 093004 (2012).
 - [12] N. Tezuka, N. Ikeda, F. Mitsuhashi, and S. Sugimoto, *Appl. Phys. Lett.* **94**, 162504 (2009).
 - [13] K. Yakushiji, K. Saito, S. Mitani, K. Takanashi, Y. K. Takahashi, and K. Hono, *Appl. Phys. Lett.* **88**, 222504 (2006).
 - [14] T. Furubayashi, K. Kodama, H. Sukegawa, Y. K. Takahashi, K. Inomata, and K. Hono, *Appl. Phys. Lett.* **93**, 122507 (2008).
 - [15] Y. Sakuraba, K. Izumi, T. Iwase, S. Bosu, K. Saito, K. Takanashi, Y. Miura, K. Futatsukawa, K. Abe, and M. Shirai, *Phys. Rev. B* **82**, 094444 (2010).
 - [16] J. Sato, M. Oogane, H. Naganuma, and Y. Ando, *Appl. Phys. Express* **4**, 113005 (2011).

- [17] M. J. Carey, S. Maat, S. Chandrashekariah, J. A. Katine, W. Chen, B. York, and J. R. Childress, *J. Appl. Phys.* **109**, 093912 (2011).
- [18] X. Y. Dong, C. Adelman, J. Q. Xie, C. J. Palmström, X. Lou, J. Strand, P. A. Crowell, J.-P. Barnes, and A. K. Petford-Long, *Appl. Phys. Lett.* **86**, 102107 (2005).
- [19] M. Ramsteiner, O. Brandt, T. Flissikowski, H. T. Grahn, M. Hashimoto, J. Herfort, and H. Kostial, *Phys. Rev. B* **78**, 121303(R) (2008).
- [20] T. Akiho, J. Shan, H.-x. Liu, K.-i. Matsuda, M. Yamamoto, and T. Uemura, *Phys. Rev. B* **87**, 235205 (2013).
- [21] S. Ishida, S. Fujii, S. Kashiwagi, and S. Asano, *J. Phys. Soc. Jpn.* **64**, 2152 (1995).
- [22] S. Picozzi, A. Continenza, and A. J. Freeman, *Phys. Rev. B* **66**, 094421 (2002).
- [23] I. Galanakis, P. H. Dederichs, and N. Papanikolaou, *Phys. Rev. B* **66**, 174429 (2002).
- [24] P. J. Webster, *J. Phys. Chem. Solids* **32**, 1221 (1971).
- [25] M. Yamamoto, T. Marukame, T. Ishikawa, K.-i. Matsuda, T. Uemura, and M. Arita, *J. Phys. D* **39**, 824 (2006).
- [26] T. Ishikawa, S. Hakamata, K.-i. Matsuda, T. Uemura, and M. Yamamoto, *J. Appl. Phys.* **103**, 07A919 (2008).
- [27] S. Tsunegi, Y. Sakuraba, M. Oogane, K. Takahashi, and Y. Ando, *Appl. Phys. Lett.* **93**, 112506 (2008).
- [28] T. Miyajima, M. Oogane, Y. Kotaka, T. Yamazaki, M. Tsukada, Y. Kataoka, H. Naganuma, and Y. Ando, *Appl. Phys. Express* **2**, 093001 (2009).
- [29] W. Wang, E. Liu, M. Kodzuka, H. Sukegawa, M. Wojcik, E. Jedryka, G. H. Wu, K. Inomata, S. Mitani, and K. Hono, *Phys. Rev. B* **81**, 140402(R) (2010).
- [30] G.-f. Li, T. Taira, K.-i. Matsuda, M. Arita, T. Uemura, and M. Yamamoto, *Appl. Phys. Lett.* **98**, 262505 (2011).
- [31] Y. Miura, H. Uchida, Y. Oba, K. Nagao, and M. Shirai, *J. Phys.: Condens. Matter* **19**, 365228 (2007).
- [32] Y. Miura, H. Uchida, Y. Oba, K. Abe, and M. Shirai, *Phys. Rev. B* **78**, 064416 (2008).
- [33] S. Picozzi, A. Continenza, and A. J. Freeman, *Phys. Rev. B* **69**, 094423 (2004).
- [34] Y. Miura, K. Nagao, and M. Shirai, *Phys. Rev. B* **69**, 144413 (2004).
- [35] I. Galanakis, K. Özdoğan, B. Aktaş, and E. Şaşıoğlu, *Appl. Phys. Lett.* **89**, 042502 (2006).
- [36] B. Hülsen, M. Scheffler, and P. Kratzer, *Phys. Rev. B* **79**, 094407 (2009).
- [37] T. Saito, T. Katayama, T. Ishikawa, M. Yamamoto, D. Asakura, and T. Koide, *Appl. Phys. Lett.* **91**, 262502 (2007).
- [38] L. G. Parratt, *Phys. Rev.* **95**, 359 (1954).
- [39] P. M. Voyles, J. L. Grazul, and D. A. Muller, *Ultramicroscopy* **96**, 251 (2003).
- [40] W. Kohn and N. Rostoker, *Phys. Rev.* **94**, 1111 (1954).
- [41] H. Akai and P. H. Dederichs, *Phys. Rev. B* **47**, 8739 (1993).
- [42] M. Rasolt and D. J. W. Geldart, *Phys. Rev. B* **34**, 1325 (1986).
- [43] T. Ishikawa, N. Itabashi, T. Taira, K.-i. Matsuda, T. Uemura, and M. Yamamoto, *J. Appl. Phys.* **105**, 07B110 (2009).
- [44] C. Pfleiderer, J. Boeuf, and H. v. Löhneysen, *Phys. Rev. B* **65**, 172404 (2002).
- [45] S. Fujii, S. Ishida, and S. Asano, *J. Phys. Soc. Jpn.* **64**, 185 (1995).
- [46] M. B. Stearns, *J. Magn. Magn. Mater.* **5**, 167 (1977).
- [47] S. Ikeda, J. Hayakawa, Y. Ashizawa, Y. M. Lee, K. Miura, H. Hasegawa, M. Tsunoda, F. Matsukura, and H. Ohno, *Appl. Phys. Lett.* **93**, 082508 (2008).
- [48] H.-x. Liu, Y. Honda, T. Taira, T. Uemura, F. Shi, P. M. Voyles, Y. Miura, M. Shirai, and M. Yamamoto (unpublished).
- [49] T. Ishikawa, N. Itabashi, T. Taira, K.-i. Matsuda, T. Uemura, and M. Yamamoto, *Appl. Phys. Lett.* **94**, 092503 (2009).
- [50] Y. Honda, H.-x. Liu, T. Uemura, and M. Yamamoto (unpublished).
- [51] S. Zhang, P. M. Levy, A. C. Marley, and S. S. P. Parkin, *Phys. Rev. Lett.* **79**, 3744 (1997).